Bioethanol Combustion in an Industrial Gas Turbine Combustor: Simulations and Experiments

Joost L. H. P Sallevelt[1]
Department of Energy Technology,
University of Twente,
Enschede 7522 NB, Netherlands
e-mail: j.l.h.p.sallevelt@utwente.nl

Artur K. Pozarlik
Department of Energy Technology,
University of Twente,
Enschede 7522 NB, Netherlands

Martin Beran
OPRA Turbines,
Hengelo 7554 TS, Netherlands

Lars-Uno Axelsson
OPRA Turbines,
Hengelo 7554 TS, Netherlands

Gerrit Brem
Department of Energy Technology,
University of Twente,
Enschede 7522 NB, Netherlands

Combustion tests with bioethanol and diesel as a reference have been performed in OPRA's 2 MWe class OP16 gas turbine combustor. The main purposes of this work are to investigate the combustion quality of ethanol with respect to diesel and to validate the developed CFD model for ethanol spray combustion. The experimental investigation has been conducted in a modified OP16 gas turbine combustor, which is a reverse-flow tubular combustor of the diffusion type. Bioethanol and diesel burning experiments have been performed at atmospheric pressure with a thermal input ranging from 29 to 59 kW. Exhaust gas temperature and emissions (CO, CO_2, O_2, NO_x) were measured at various fuel flow rates while keeping the air flow rate and air temperature constant. In addition, the temperature profile of the combustor liner has been determined by applying thermochromic paint. CFD simulations have been performed with ethanol for five different operating conditions using ANSYS FLUENT. The simulations are based on a 3D RANS code. Fuel droplets representing the fuel spray are tracked throughout the domain while they interact with the gas phase. A liner temperature measurement has been used to account for heat transfer through the flame tube wall. Detailed combustion chemistry is included by using the steady laminar flamelet model. Comparison between diesel and bioethanol burning tests show similar CO emissions, but NO_x concentrations are lower for bioethanol. The CFD results for CO_2 and O_2 are in good agreement, proving the overall integrity of the model. NO_x concentrations were found to be in fair agreement, but the model failed to predict CO levels in the exhaust gas. Simulations of the fuel spray suggest that some liner wetting might have occurred. However, this finding could not be clearly confirmed by the test data. [DOI: 10.1115/1.4026529]

1 Introduction

To reduce the consumption and emissions of fossil fuels, the interest in the application of biofuels for the generation of power and heat is growing. This trend will result in the need for gas turbine combustors that are capable of handling nonconventional fuels, which often have different physical and chemical properties from those of fossil fuels. It is therefore important to investigate how the use of such novel fuels affects the quality of combustion.

Among the biofuels that are considered to be applicable in gas turbine engines, bioethanol is seen as a very promising alternative. Bioethanol is currently the most widely used biofuel in the world as it has been employed as a transportation fuel since many decades, in both blended and pure form [1]. An increasing interest to study the possibilities of its application in gas turbines to produce power and heat on a larger scale in a sustainable manner can be seen.

It must be noted that bioethanol is identical to ethanol from a chemical point of view; the only difference is that bioethanol comes from a biological source. In literature only little data is available regarding the combustion behavior of pure ethanol in gas turbines. However, the few experimental studies conducted so far confirm the technical feasibility. Tests with ethanol in a 2.5 MW industrial gas turbine were conducted at various loads [2,3]. The equipment ran stably and the normalized CO and NO_x emissions were measured to be low for all conditions. Emissions of SO_2 were negligible, as sulfur is naturally absent in bioethanol.

These results are in agreement with the findings of Moliere et al. [4], who carried out a preliminary characterization of the combustion of naphtha/bioethanol blends with up to 95% ethanol. All blends showed excellent combustion performances, with low NO_x emissions and virtually zero emissions of CO, UHC, and SO_x.

To reduce the relatively high cost associated with anhydrous ethanol, Breaux and Acharya [5] studied the effect of elevated water content on swirl-stabilized ethanol/air flames. Their test results indicated that hydrous ethanol with up to 20% water can be used for continuous flame applications. The water reduced the peak flame temperatures and, therefore, also NO_x emissions, while negative effects on combustion efficiency or flame stability were measured to be insignificant.

A numerical study has been performed by Laranci et al. [6] to investigate bioethanol as a fuel for a micro gas turbine with an annular combustion chamber. Ethanol enters the computational domain as droplets with dimension of 120 μm, after which the fluid dynamics and vaporization are tracked by a Lagrangian multiphase model. The article reports preliminary simulation results in terms of temperatures, pressures and emissions. These results have not been validated because experimental data from the combustion chamber was only available for natural gas combustion. Nevertheless, there seem to be inconsistencies in the calculated emission data, so that the reliability of the presented preliminary data can be questioned.

In the present study, the application of bioethanol as a biomass-derived fuel has been examined both numerically and experimentally in OPRA's 2 MWe class OP16 gas turbine combustor. Measurements with diesel fuel at similar operating conditions serve as a reference. A commercial CFD code is used to simulate the ethanol combustion process at different operating points based on reduced chemical kinetics. Experiments in an atmospheric test

---

rig have been performed to evaluate the combustion quality of bioethanol and to obtain data for validation of the CFD results.

2 Experimental Method

Bioethanol spray combustion has been studied in a modified OP16 gas turbine combustor mounted in a test rig. A scheme of the test rig and the location of the sensors is shown in Fig. 1. Thermocouples are used to measure the temperature of the injected fuel, the inlet air and the exhaust gases. The pressure sensor in the top left is used to measure the pressure loss in the combustor. Continuous samples were taken from the exhaust gas to measure its composition during the tests. Concentrations of CO_2 and O_2 have been determined with an ADC 5000 analyzer, oxides of nitrogen with a Thermo Model 42C and CO levels with a Thermo Model 48C.

The experimental procedure started by establishing a stable air flow of $420\,m^3/h$. at a constant temperature. After preheating of the setup by burning fuel for at least 15 min, a series of experiments have been performed at atmospheric pressure with a thermal input ranging from 29 to 59 kW. Once steady state conditions were reached at a certain fuel flow rate, all sensor data was logged using data acquisition software and emissions were read from the gas analyzer displays.

In addition, the temperature profile on the liner has been determined for 43 kW bioethanol combustion by applying thermochromic paint. To assure an adequate sensitivity of the paint to temperature changes, several different types of paint have been applied. The paint colors have been visually inspected to determine the temperature range at each location on the liner surface.

The air flow, fuel flow and combustor inlet temperature were measured with an accuracy of $\pm0.7\%$, $\pm2.4\%$ and $\pm1.5\%$, respectively. The calibration sheet of the exhaust gas thermocouples reports a maximum error of $\pm0.27\%$. However, these thermocouples were not shielded during the measurements. Comparative tests with a shielded thermocouple showed that the unshielded sensors give up to 10% higher values due to radiation from the flame. The emissions have been analyzed with an estimated accuracy of ±0.25 pp for CO_2, ±0.5 pp for O_2 and ±2 ppmv for both NO_x and CO.

3 Numerical Model

The numerical study has been performed by using the Euler–Lagrange approach in ANSYS FLUENT [7]. In this approach, the fuel spray is considered as a discrete liquid phase traveling in a continuous gas phase. Parcels, representing fuel droplets with similar properties, are tracked throughout the domain while they interact with the surrounding gas. The RANS equations governing the gas phase are coupled with a nonpremixed combustion model to include detailed flame chemistry. The models describing the gas phase, fuel spray and chemical reactions are discussed in the following sections.
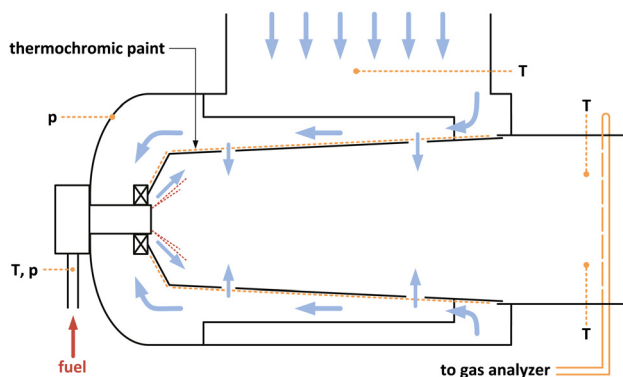
3.1 Computational Domain. In order to limit the computational cost, a 45 deg slice of the combustor geometry is taken as the flow domain. The combustor is not fully rotationally symmetric, however, because the number of circumferentially distributed air admission holes are not always divisible by 8 at all axial locations. Hence, the original geometry had to be modified to allow for the use of periodic boundary conditions in the CFD code. The required symmetry was achieved by changing the number of air admission channels at two locations in the nozzle from 7 to 8 and from 14 to 16, respectively. The total inlet area of these flow passages has been preserved to minimize the influence of these changes on the air split. Since the nozzle air streams are collected in shared volumes first, any differences in the local flow field inside the nozzle will be hardly noticeable at the nozzle outlet annuli. The computational domain is extended by 50 mm to reduce the effect of the outlet boundary condition in the calculations.

The domain has been spatially discretized using an unstructured tetrahedral grid with two to three layers of prisms at the flow boundaries. Three grids have been tested to examine grid dependency of the solution. The coarse, medium and fine grid, respectively, consisted out of 1.45, 2.60 and 3.21×10^6 cells. In all grids, 8 to 12 cells were used across the width of a channel or hole.

Comparison of the velocity and temperature profiles showed that a cell size of 1.3% of the liner diameter is needed to capture the steep gradients near the walls, whereas twice this cell size is sufficient for the core of the domain. According to this information, a final grid consisting of 2.28×10^6 cells (see Fig. 2) provides the best trade-off between resolution and computation time.

3.2 Gas Phase. Chemically reacting turbulent flows are mathematically described by the conservation equations for mass, momentum, species and enthalpy. The density-weighted time-averaged Navier–Stokes equations are solved to obtain the solution of the mean turbulent flow field.

The Reynolds stresses and the species and enthalpy turbulent fluxes are closed using the shear stress transport (SST) $k-\omega$ turbulence model. In case of swirling flows, the SST $k-\omega$ model developed by Menter [8] generally shows good performance [9] at modest computational cost. The model combines the advantages of the $k-\omega$ model, which is more robust and accurate in the near-wall region, with the $k-\varepsilon$ model, which is preferred in the far field zones away from the surface. Blending functions are employed to add these two models together.

Heat transfer by nonluminous radiation has been included in the calculations by using the discrete ordinates (DO) model [7]. This type of radiation is due to presence of certain heteropolar gases, mainly carbon dioxide and water vapor. Scattering caused by gas molecules has been neglected, because it does not play a major role in radiative heat transfer [10]. The value of the absorption coefficient depends on the composition of the gas mixture and is computed using the weighted-sum-of-gray-gases model [7]. This model evaluates the local value of the radiation absorption coefficient as function of the local mass fractions of water vapor and carbon dioxide. Luminous radiation depends on the number and size of the solid particles (mainly soot) in the flame. Since soot production in the flame is not modeled, luminous radiation is neglected.
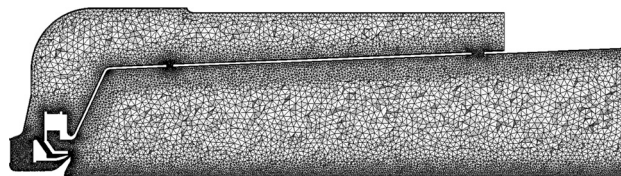

Fig. 1   Scheme of the test rig and the location of sensors

Fig. 2   Final grid used for the simulations

The walls of the combustion chamber participate in the internal heat transfer via both convection and radiation. It is assumed that the absorptivity of the walls is equal to the emissivity, and that the reflected and emitted radiation from the surfaces is fully diffuse.

3.3 Fuel Spray.

Despite intensive research over the past decades, the atomization process is still not well understood [11]. The physics governing the spray characteristics are very complex and, especially in the dense spray region, are challenging to investigate with current experimental techniques. Most studies therefore start with the atomized spray by imposing a distribution of droplet sizes as an inlet condition for the simulations.

Also in this study, the most complex phenomena taking place in the dense spray region are not captured in the model. Instead, the fuel is injected into the combustor in the form of droplets according to a Rosin–Rammler distribution. Here, the Lagrangian formulation has the advantage that the representation of the imposed distribution is relatively easy, because different properties can be assigned to each parcel injected.

Once the parcels are injected in the shape of a hollow cone, only secondary breakup needs to be considered. According to Faeth et al. [12], this process can take place in different modes depending on the Weber number and Ohnesorge number

$$\text{We} = \frac{\rho_g u_r^2 D_p}{\sigma} \quad \text{Oh} = \frac{\mu_p}{\sqrt{\rho_p D_p \sigma}} \tag{1}$$

where u_r is the velocity of the droplet relative to the gas, D_p is the droplet diameter, σ is the surface tension and the subscripts g and p denote properties of the gas phase and the droplet, respectively. The Ohnesorge number is the ratio between the viscous forces and surface tension forces. Experimental research has shown that viscous forces are insignificant if $\text{Oh} < 0.1$ [12]. The estimated Ohnesorge number in the present study will be lower than this value, so that breakup is virtually not influenced by viscous damping of the liquid. The breakup mode is therefore only described by the Weber number, which determines the ratio between the disruptive aerodynamic force and the restorative surface tension force. The maximum Weber number is estimated to be 16, which means that secondary atomization might take place by means of bag breakup. Breakup at these low Weber numbers can be modeled with rather good accuracy using the TAB model developed by O'Rourke and Amsden [7].

The trajectory of a particle or droplet in a carrier fluid is predicted by integrating the force balance over a single dispersed phase particle. In case the particles concern small droplets in a gas turbine combustor, it may be assumed that the density of the droplet is much larger than that of the fluid, that the droplet size is small compared to the turbulence integral length scale and that the effect of shear on droplet motion is negligible [13]. Furthermore, gravity and buoyancy effects can be neglected compared to drag forces. The drag coefficient is calculated from the dynamic drag model, in which the drag depends on the flow regime around the droplet and the droplet shape. The random effects of turbulence on particle dispersion are included by using the discrete random walk model [7].

When modeling a particle-laden flow, it is important to examine the extent of coupling between the discrete and continuous phase [14]. In most fuel sprays, the local liquid volume fraction is close to 1 near the orifice of the atomizer and decreases downstream due to disintegration and atomization of the liquid structure [15]. According to a study by Faeth et al. [12], a pressure-atomized spray in still gases after primary breakup can be considered as a dilute environment, where effects of droplet collisions are negligible. This observation is supported by Merci et al. [11], who found that a spray becomes diluted beyond the liquid core, with liquid volume fractions less than about 1%. Following these observations the dispersed spray can be modeled using two-way coupling

of turbulence, thereby disregarding any interactions between droplets.

Evaporation of the fuel is calculated using a diffusion-based model. Here, the mass flux at the droplet surface is evaluated by assuming that the partial pressure of vapor at the interface is equal to the saturated vapor pressure [7]. The diffusion coefficient of ethanol vapor in air is configured as a function of the droplet film temperature using the 1/3 averaging rule. In case a droplet hits the hot flame tube, it is assumed that the fuel is released instantaneously.

The importance of radiation absorption by fuel droplets relative to convective heat transfer depends primarily on the type of fuel, the temperature of the flame and the droplet size. Faeth [16] states that previous studies have shown that radiation effects are relatively unimportant for droplet sizes representative for most fuel sprays. This conclusion is in accordance with the results of Tseng and Viskanta [17] and Godsave [18], and therefore in the present study radiative heating has been ignored for these small sizes.

3.4 Droplet Size Distribution.

Injection of the fuel in the form of droplets requires a definition of the initial droplet size as an input parameter. However, because atomization is a random process, the droplets formed after primary breakup are not uniform in size. To account for these variations, it is assumed that the droplet size obeys a Rosin–Rammler distribution [19]

$$1 - F = e^{-\left(D_p/\overline{D}\right)^q} \tag{2}$$

where F is the volume fraction of the droplets with a diameter smaller than D_p. The distribution is defined by a characteristic mean diameter $\overline{D}$ and the spread parameter q. Here, $\overline{D}$ is the droplet diameter for which $1 - F = e^{-1}$ or, equivalently, $F = 0.632$. The parameter q is a measure for the spread in the droplet size.

Experimental data on the droplet size distribution of the spray produced by the prefilming airblast nozzle in the combustor are not available. Hence, empirical correlations have been used to estimate the two parameters required for defining the spray. A representative value for $\overline{D}$ can be found by first estimating the Sauter mean diameter (SMD). This parameter is defined as the total spray volume divided by the total surface area of all droplets. Research on the performance of prefilming airblast atomizers has been conducted by El-Shanawany and Lefebvre [20]. Based on their drop size measurements using a wide variety of liquids at representative atomizing conditions for this study, they proposed a practical correlation to estimate the SMD

$$\text{SMD} = 0.073 \left(\frac{\sigma}{\rho_a U_a^2}\right)^{0.6} \left(\frac{\rho_f}{\rho_a}\right)^{0.1} D_{pf}^{0.4} \left(1 + \frac{1}{\text{ALR}}\right)$$
$$+ 0.015 \left(\frac{\mu_f^2 D_{pf}}{\sigma \rho_f}\right)^{0.5} \left(1 + \frac{1}{\text{ALR}}\right) \tag{3}$$

In Eq. (3), D_{pf} is the diameter of the prefilmer, U denotes the velocity and ALR is the air-to-liquid mass ratio. The subscripts f and a refer to fuel and air, respectively. Under the assumption that the variation in droplet size can be described by Eq. (2), the SMD is uniquely related to $\overline{D}$. The relation between these two characteristic diameters can be found in Liu [21] and reads

$$\overline{D} = \text{SMD} \cdot \Gamma(1 - 1/q) \tag{4}$$

A representative value for q is estimated based on experimental data found in Lefebvre [22] for an airblast atomizer at different atomizing air velocities. Values of q varying from 3.35 to 3.6 are reported for a water spray at air speeds ranging from 54.8 to 122 m/s. Interpolation gives a spread parameter of about 3.4 at an air velocity of 60 m/s, characteristic for the atomizer conditions in the bioethanol tests. Although the effect of the differences

Table 1 Operating conditions in the five simulated cases

Case	Overall ER	Air flow[a] (m^3/h)	Fuel flow (g/s)	Power[b] (kW)
1	0.15	328	0.975	26
2	0.20	328	1.3	35
3	0.25	328	1.625	44
4	0.30	328	1.95	53
5	0.35	328	2.275	61

[a]Corrected for 22% leak air measured in the test rig.
[b]Based on a lower heating value of 27 MJ/kg.

between the properties of water and ethanol is unclear, the reported value is used as an estimation for the spread diameter of the ethanol spray.

The droplet size distribution resulting from Eqs. (2)–(4) differs for each case in Table 1. As an example, the differential distribution curve for Case 3 (SMD = 44 μm) is shown in Fig. 3.

3.5 Nonpremixed Combustion Modeling. Solving the species conservation equations for all species involved in detailed chemistry calculations rapidly exceeds computational limits. For this reason, combustion is modeled following the flamelet approach. The general idea is to decompose the combustion problem into two subproblems: mixing and flame structure. The mixing problem is related to the mixing processes of the fuel and oxidizer streams, and therefore treats all aspects related to the flow field. The flame structure problem involves linking the mixing state to the flame variables; thus describing the combustion process.

Departure from chemical equilibrium due to straining of the flame is characterized by the scalar dissipation rate at the flame location. This parameter essentially accounts for the influence of mixing on the flame structure. In addition, the effect of heat loss or heat gain on the flame temperature has been incorporated by using nonadiabatic flamelets. The actual flame temperature is obtained by correcting the adiabatic flame temperature based on the enthalpy level as calculated from the enthalpy balance equation.

The chemical reactions have been preprocessed using a reduced mechanism for ethanol oxidation proposed by Roehl and Peters [23]. This mechanism includes 38 species and 228 reactions. The nonadiabatic, steady flamelets have been calculated for different scalar dissipation rates up to the rate at which the flame is extinguished. Average values of the flame variables are then computed and tabulated for different enthalpy levels. The variables stored in the PDF tables are temperature, species mass fraction and density.
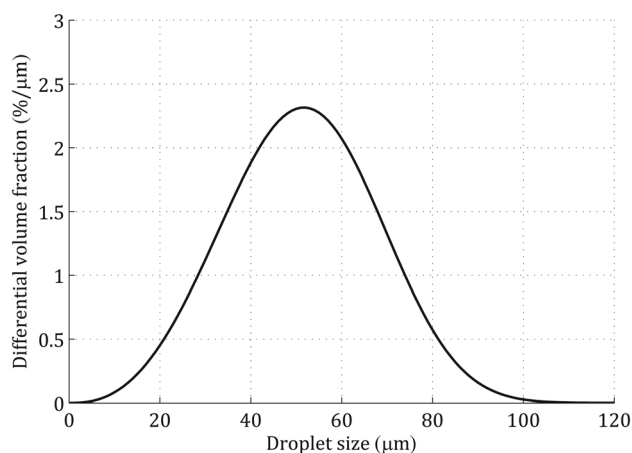
Formation of thermal NO is predicted by the extended Zeldovich mechanism [7]. The species concentrations required to calculate the formation rates are obtained from the solution of the combustion model.

3.6 Boundary Conditions. A mass flow rate and temperature condition are specified at the inlet. The air flow of 420 m^3/h during the combustion tests has been corrected for the leak air at the connection between the liner and the exhaust duct. The leak air was measured to be 22% of the total air flow at cold conditions. The inlet temperature corresponds to the value at which the air leaves the compressor stage in the gas turbine. It is assumed that the turbulence intensity at the inlet is 5%. This parameter can be used to determine the turbulence parameters k and ω. At the outlet, the relative static pressure is set to zero. The fuel flow rate has been varied to make a comparison at different thermal inputs. The operating conditions for the five simulated cases are defined in Table 1.

The temperature on the outer surface of the liner at base conditions has been determined experimentally using thermochromic paint. Visual inspection of the colors resulted in local upper and lower temperature limits. A representative temperature profile for use in CFD is obtained by approximating the mean values of each range indicated by the paint. The dimensionless temperature limits and the profile for the purpose of CFD are shown in Fig. 4. Although the liner temperature may vary with thermal input, this profile has been imposed on the outer liner surface in all simulations to estimate the heat flux through the flame tube. On the inner surface, a heat flux is prescribed such that the energy balance is not violated.

An emissivity of 0.7 has been assumed for the (oxidized) inner liner surface and 0.6 was chosen for the remaining surfaces [10,24]. The walls of the outer casing are considered adiabatic to model the thick layer of insulation around the combustor in the test rig. The liner extension is set to adiabatic. To more closely approximate the open space behind the outlet, a free slip condition has been applied on the extended part of the liner.

3.7 Numerical Procedure. The numerical solution presented in this paper has been computed using a pressure-based coupled AMG solver. Next to explicit under-relaxation factors, a pseudo transient technique has been employed as a form of implicit under-relaxation to stabilize the solver while the solution is calculated. The PRESTO! scheme has been selected as the pressure interpolation scheme.

Quantities at cell faces are interpolated from the center values using a second order upwind scheme, except for velocities. For the momentum equation, a first order scheme was used in order to achieve convergence by damping out strong oscillations in the flow. The effect of this setting on the flow field has been evaluated by comparing cold flow simulations. Changing the discretization
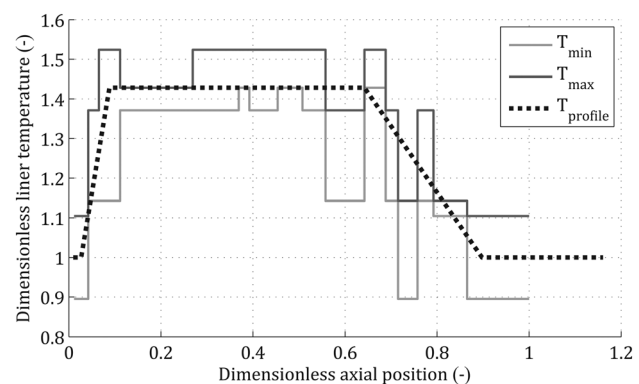

Fig. 3 Calculated droplet size distribution curve for the ethanol spray in Case 3

Fig. 4 Dimensionless liner temperature limits from the paint test and the profile used for CFD

scheme for only the momentum equation into first order did not lead to significant differences in air split. The difference in air split between the schemes regarding atomization air is 2%, for swirler air 3%, for primary air 0% and for dilution air 0.4%. The overall flow pattern did not change either, but the velocity profiles measured along the flame tube radius generally showed an underestimation of the recirculation strength. In the primary zone, however, the flow fields predicted by the different methods are in fairly good agreement. Since the phenomena of interest mainly take place in this region, the discretization error of the velocities is considered to be acceptable.

4 Results and Discussion

In this section, the results from the simulations and combustion tests with ethanol are reported and compared. In addition, the test results for ethanol are compared with the results for diesel as a reference fuel. Adiabatic flame temperatures (AFT) and compositions following from a complete combustion reaction (CCR) are included in the graphs to check the integrity of the simulations and the combustion efficiency during the experiments.

The experimental data have been time-averaged over more than 30 s with a sampling interval of 0.1 s. The measurement locations are indicated in Fig. 1. Simulation results have been obtained at the outlet of the computational domain, which is located 40 mm upstream of the position of the sensors in the test rig. The normalized overall imbalance of mass and heat in the converged solutions is found to be less than 0.002% and 3%, respectively. Here, the total mass flow and thermal input are used for normalization.

Figure 5 gives an impression of the flame location by showing the dimensionless temperature (Fig. 5(a)) and OH mole fraction contours (Fig. 5(b)) inside the combustor for Case 3. Due to the strong recirculation and swirl in the primary zone, the flame is forced to the outer region of the flame tube, close to the wall. The liner is cooled by the fresh air from the compressor and a protective air sheet originating from the swirler.

4.1 Temperatures.
A comparison of the nondimensionalized exhaust gas temperature as function of the overall equivalence ratio is shown in Fig. 6. The CFD results are slightly lower than the adiabatic flame temperatures. In terms of heat, the differences between these numerical results are in the same order as the overall energy imbalance in the CFD simulations (4.5%).

Temperatures measured in the test rig are however much lower than these calculated values. Also, a significant deviation between the measured temperatures for ethanol and diesel is observed, whereas the adiabatic temperatures are almost the same for both fuels. High heat loss from the combustor can be excluded as a major cause because of proper insulation and, as stated before, the influence of thermocouple radiation was measured to be small. Therefore, the difference must be due to the temperature gradient over the exhaust radius. This implies that the measured temperatures
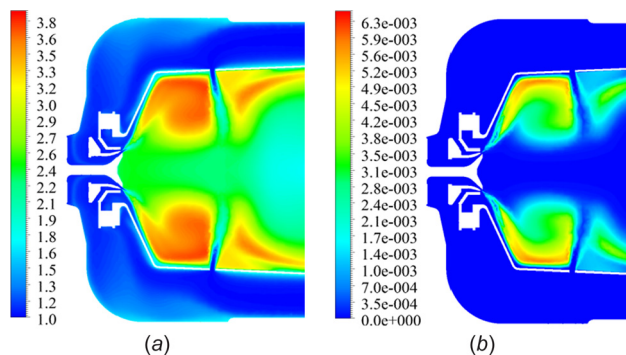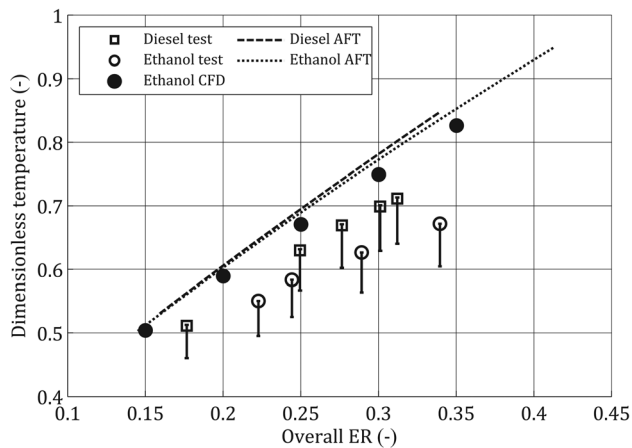

Fig. 6 Measured and calculated dimensionless exhaust gas temperatures as function of the overall equivalence ratio

are strongly dependent on the position of the thermocouples in the test rig and on the flow field corresponding to that specific operating condition.

4.2 Emissions.
The CO_2 levels as function of the equivalence ratio are given in Fig. 7. The graph illustrates a very good agreement between the calculations and the test results. This indicates that the combustion efficiency during the burning tests was very high for both ethanol and diesel. The rightmost two ethanol test results are slightly too high, but fall within the limits of uncertainty. The O_2 concentrations shown in Fig. 8 confirm that the fuels are fully combusted. The leftmost two data points from the ethanol tests are slightly deviating from the trend due to measurement inaccuracy.

The concentration of CO, nondimensionalized and normalized to 15% oxygen content, is plotted in Fig. 9. The graph shows a strong increase in CO level for equivalence ratios below 0.2. No data could be obtained for the ethanol flame at these lean conditions, because the flame became very unstable. The lean limit for diesel is expected to be lower due to the higher flame temperature. At equivalence ratios above 0.2, it can be concluded that diesel and bioethanol yield similar CO concentrations. The graph of the unburnt hydrocarbon content of the flue gas is omitted here, but shows the same trend.

CO emissions predicted by the CFD model are not shown in the graph because they were strongly underestimated over the entire range of operating conditions. Although the calculations show
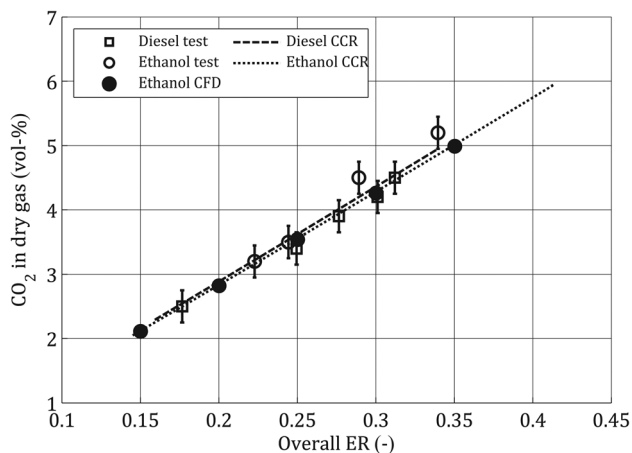

Fig. 5 Dimensionless temperature field (a) and OH field (b) in Case 3, shown on a cross section of the combustor

Fig. 7 Measured and calculated CO_2 concentration as function of the overall equivalence ratio

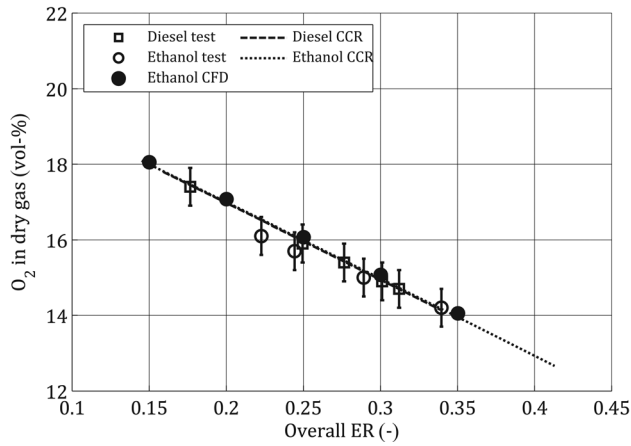**Fig. 8   Measured and calculated O$_2$ concentration as function of the overall equivalence ratio**
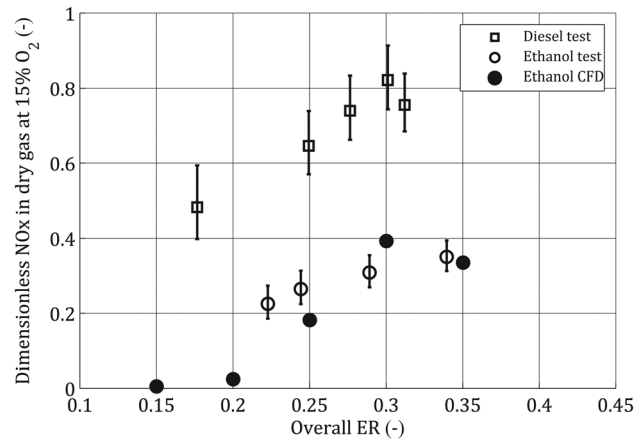

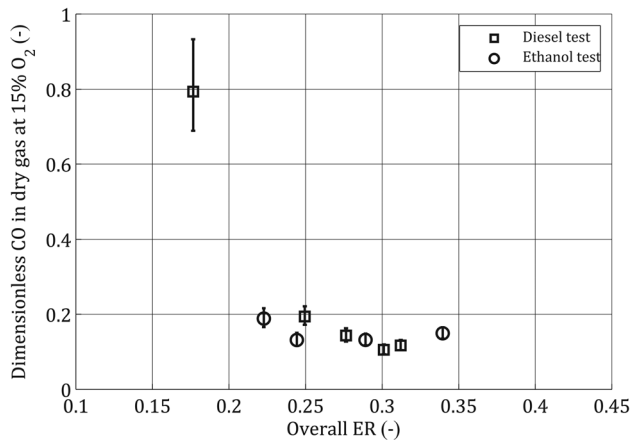**Fig. 9   Measured dimensionless CO concentration as function of the overall equivalence ratio, normalized to 15% O$_2$**

Fig. 10   Measured and calculated dimensionless NO$_x$ concentration as function of the overall equivalence ratio

A fair agreement is seen when comparing the numerical and experimental data points.

4.3   Droplet Evaporation. Simulation of the fuel spray indicates that some fuel impinges on the liner surface because the rate of evaporation is not high enough for the larger droplets. These droplets partly evaporate but eventually reach the liner, after which the remaining fuel is vaporized instantly in accordance with the boundary condition prescribed at these walls. Since the droplet life time during the tests is not exactly known, the authors can only speculate if this result is realistic.

In case this prediction is incorrect, there are three possible explanations: the initial droplet sizes are overestimated, the TAB model fails to describe the secondary breakup, or the evaporation model underpredicts the evaporation rate. The first of the aforementioned explanations is however unlikely, because the correlation of El-Shanawany yields relatively small droplet sizes compared to those obtained using other empirical correlations for prefilming airblast atomizers [25,26]. The droplet life time is highly sensitive to the initial droplet size, so the use of a different SMD correlation will generally increase the impingement of droplets significantly.

Regarding the second explanation, Gepperth et al. [26] have shown that the droplet sizes predicted by Eq. (3) can only be representative after secondary breakup. Droplet sizes resulting from primary breakup very close to the atomizer lip can actually be an order of magnitude larger. Based on this observation, it is also no surprise that secondary breakup does not occur in the simulations. This process must have occurred already for such small droplets as injected into the domain. Considering the low Weber numbers, it is also unlikely that the breakup model will have been a major cause of the wall wetting.

To get more insight into the evaporation process itself, the evolution of the droplet diameter as function of time is shown in Fig. 11. The graph reports tracking data for 10 different parcel diameters in the spray. It can be seen that droplets with an initial diameter larger than 80 μm are not completely evaporated before reaching the wall.

Evaluation of droplet temperature data over time shows that the droplets are quickly heated up to a certain equilibrium temperature. At this temperature, the heat transfer towards the droplet is equal to the evaporative cooling. Since the diffusion coefficient is high in the hot combustor environment and the heat of vaporization of ethanol is relatively large, the droplet temperature does not reach boiling point. This finding is confirmed by experimental data found in Maqua et al. [27] and Lavieille et al. [28].

In Fig. 12, the square of the droplet diameter is shown as function of time. The graph illustrates a predominantly linear relation
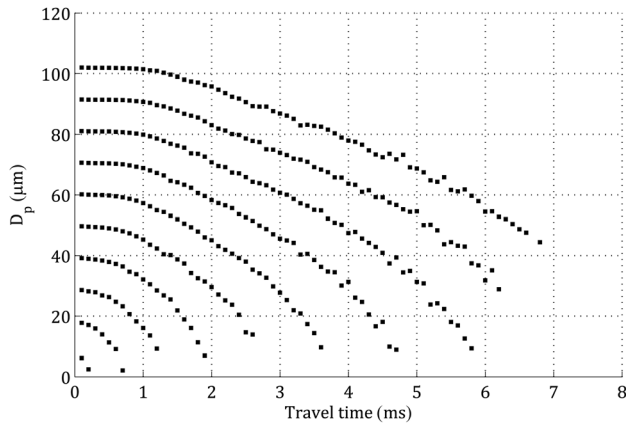
that CO is formed where combustion is in an early stage, almost all CO is consumed in subsequent reactions so that CO levels at the outlet are negligible. This deficiency is a consequence of the fast chemistry assumption behind the steady laminar flamelet model. The flame is assumed to immediately respond to the mixing state, and departure from chemical equilibrium is accounted for only as a result of aerodynamic strain. The strain rate near the exhaust is very low, so that insignificant CO levels are predicted at the sample location. Relatively slow chemical processes such as low-temperature CO oxidation cannot be described by the current combustion model. Models that include chemical nonequilibrium due to large chemical time-scales should give more accurate results, but are unfortunately not economically feasible yet.

Figure 10 shows the NO$_x$ emissions, nondimensionalized and normalized to 15% oxygen content, as function of the equivalence ratio. As expected, the concentration increases with the ER due to higher temperatures in the combustion chamber. Since the fuels do not contain nitrogen, these emissions are due to the formation of thermal or prompt NO$_x$. The test results show that NO$_x$ emissions for bioethanol are considerably lower than for diesel, with a reduction of roughly 50% over the entire range.

The CFD analysis only provides a prediction for the NO concentration. NO$_2$ emissions are not included in the Zeldovich mechanism, but can be estimated from the NO levels. The combustion tests have shown that NO accounts for about 75% of the total NO$_x$. The NO levels obtained from CFD are therefore divided by this value to make an estimation of the total NO$_x$ levels.

Fig. 11 Calculated droplet diameter as function of the droplet travel time in Case 3
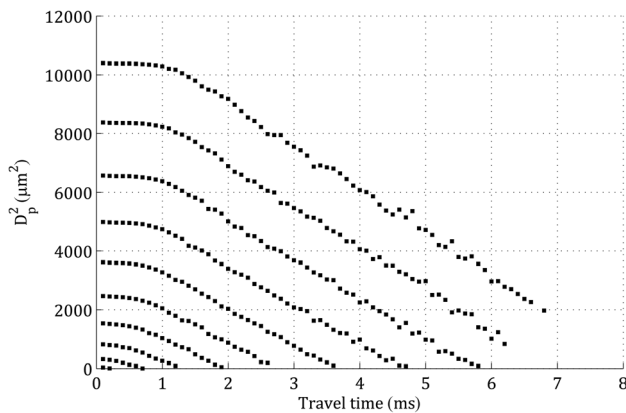

Fig. 12 Calculated square droplet diameter as function of the droplet travel time in Case 3
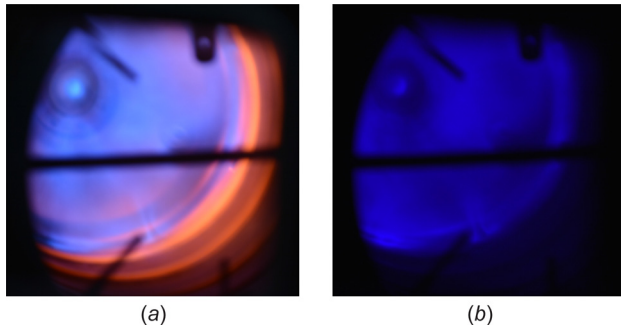

Fig. 13 Image of the ethanol flame without (a) and with (b) CH*-filter in front of the camera

between these parameters, which means the evaporation process can be approximated using the D^2-law:

$$D_p^2 = D_{p,0}^2 - \lambda_{ev} t \qquad (5)$$

where $D_{p,0}^2$ is the initial droplet diameter, t is the droplet residence time and λ_{ev} is the evaporation constant. The D^2-law is widely used to describe the evaporation of single component, spherical droplets. The evaporation constant in the current simulations can be determined from Fig. 12 and varies between $12 \cdot 10^{-7}$ and $15 \cdot 10^{-7}$ m^2/s for the droplets larger than $50\,\mu$m. Measurements on burning ethanol droplets in quiescent air have shown that λ_{ev} is

between $8.1 \cdot 10^{-7}$ m^2/s and $8.6 \cdot 10^{-7}$ m^2/s [18,29,30], but data for higher Reynolds numbers (i.e., Re $= 10 - 100$) has not been found. The relatively high values for λ_{ev} seen in the CFD model can be expected due to the effect of convection around the droplets, but more data on droplet evaporation in convective flows is required to properly verify the evaporation model in this case.

In case severe wall wetting occurred during the combustion tests, the formation of a liquid film may be visible in the liner temperature profile. The thermochromic paint does however not indicate unexpected liner temperatures in the primary zone (Fig. 4). Nevertheless, this result should not be regarded as conclusive either, since the simulation shows there is only a small fraction of the total fuel flow that impinges the liner at these conditions. It is besides not obvious that a strong relation between wall wetting on the inside and the temperature on the outside exists.

In an effort to verify the simulated droplet behavior in a different way, the ethanol flame has been photographed as shown in Fig. 13. These pictures have been taken via a mirror that was mounted behind the exhaust duct. To improve the visibility of the flame seen in Fig. 13(a), the chemiluminescence of CH radicals (CH*) was captured by using a bandpass filter (430 ± 2 nm) to get Fig. 13(b). The image illustrates that the flame front reaches up to the liner, suggesting the presence of fuel at this location.

When also considering the CFD results, the authors conclude that some wall wetting may have occurred in some minor and allowable extent. No clear reason has been found to question the evaporation model used in the current study.

5 Conclusions

In this work, combustion of bioethanol has been studied in a modified OP16 industrial gas turbine combustor. Combustion tests have been performed with a thermal input ranging from 29 to 59 kW. The measurements with ethanol have been compared with the combustor performance on diesel fuel and with results from CFD.

The test data show that bioethanol has been fully combusted. CO emissions are found to be similar, but NO$_x$ levels are considerably lower compared to diesel.

CFD predictions of the CO$_2$ and O$_2$ levels in the exhaust gas are in good agreement with the experimental results. The trend of the NO$_x$ emissions is captured with fair accuracy. The current chemistry model is however incapable of predicting CO emissions. Exhaust gas temperatures deviate significantly from the test results. This is probably caused by incomplete mixing of flue gases at the outlet of the combustor. When compared to adiabatic flame calculations, the temperatures from CFD show a close match.

According to the CFD model, the droplet evaporation rate is too low to prevent impingement of droplets onto the liner surface. Chemiluminescence of CH radicals in the flame front indicated that the flame extends up to the liner, suggesting the presence of fuel near the surface. However, this result was not confirmed by liner temperature measurements using thermochromic paint. Also, experimental data on burning ethanol droplets proved to be insufficient to draw hard conclusions on this point.

Nomenclature

$\overline{D}$ = characteristic droplet diameter
D_p = droplet diameter
$D_{p,0}$ = initial droplet diameter
D_{pf} = diameter of the prefilmer
F = cumulative volume fraction
q = droplet size spread parameter

U_a = air velocity
u_r = velocity of the droplet relative to the gas

Greek Symbols

λ_{ev} = evaporation constant
μ_f = dynamic viscosity of the fuel
μ_p = dynamic viscosity of the droplet
ρ_a = air density
ρ_f = fuel density
ρ_g = gas density
ρ_p = droplet density
σ = surface tension

Abbreviations

AFT = adiabatic flame temperature
ALR = air-to-liquid mass ratio
CCR = complete combustion reaction
ER = equivalence ratio
Oh = Ohnesorge number
pp = percentage points
ppmv = parts per million by volume
SMD = Sauter mean diameter
We = Weber number

References

[1] Balat, M., and Balat, H., 2009, "Recent Trends in Global Production and Utilization of Bio-Ethanol Fuel," Appl. Energy, **86**(11), pp. 2273–2282.
[2] Lupandin, V., Thamburaj, R., and Nikolayev, A., 2005, "Test Results of the OGT2500 Gas Turbine Engine Running on Alternative Fuels: BioOil, Ethanol, BioDiesel and Crude Oil," ASME Turbo Expo 2005, Reno, NV, June 6–9, ASME Paper No. GT2005-68488, pp. 421–426.
[3] Razbin, V., and Coyle, I., 2004, "Emissions Tests on Magellan Aerospace Orenda Corporation, OGT 2500 Gas Turbine," CETC Energy Technology Centre, Ottawa, Canada, Report No. CETC-O-ACT-04-043-1 (CF).
[4] Moliere, M., Vierling, M., Aboujaib, M., Patil, P., Eranki, A., Campbell, A., Trivedi, R., Nainani, A., Roy, S., and Pandey, N., 2009, "Gas Turbines in Alternative Fuel Applications: Bio-Ethanol Field Test," ASME Turbo Expo 2009, Orlando, FL, June 8-12, ASME Paper No. GT2009-59047, pp. 341–348.
[5] Breaux, B. B., and Acharya, S., 2013, "The Effect of Elevated Water Content on Swirl-Stabilized Ethanol/Air Flames," Fuel, **105**, pp. 90–102.
[6] Laranci, P., Bidini, G., Fantozzi, F., and Desideri, U., 2013, "CFD Analysis of an Annular Micro Gas Turbine Combustion Chamber Fuelled With Liquid Biofuels: Preliminary Results With Bioethanol," ASME Turbo Expo 2013, San Antonio, TX, June 3–7, ASME Paper No. GT2013-95696.
[7] Fluent Inc., 2006, Fluent 6.3 User's Guide, Fluent Inc., Lebanon, NH.
[8] Menter, F., 1994, "Two-Equation Eddy-Viscosity Turbulence Models for Engineering Applications," AIAA J., **32**(8), pp. 1598–1605.
[9] Engdar, U., and Klingmann, J., 2002, "Investigation of Two-Equation Turbulence Models Applied to a Confined Axis-Symmetric Swirling Flow," ASME Pressure Vessels and Piping Conference, Vancouver, BC, Canada, August 5–9, ASME Paper No. PVP2002-1590, pp. 199–206.
[10] Cengel, Y., 2007, Heat and Mass Transfer: A Practical Approach, 3rd ed., McGraw-Hill, Boston, MA.
[11] Merci, B., Roekaerts, D., and Sadiki, A., 2011, Experiments and Numerical Simulations of Diluted Spray Turbulent Combustion: Proceedings of the 1st International Workshop on Turbulent Spray Combustion, Vol. 17, Springer, New York.
[12] Faeth, G. M., Hsiang, L. P., and Wu, P. K., 1995, "Structure and Breakup Properties of Sprays," Int. J. Multiphase Flow, **21**(S), pp. 99–127.
[13] Moin, P., and Apte, S. V., 2006, "Large-Eddy Simulation of Realistic Gas Turbine Combustors," AIAA J., **44**(4), pp. 698–708.
[14] Ranade, V., 2001, Computational Flow Modeling for Chemical Reactor Engineering, Vol. 5, Academic, New York.
[15] Ashgriz, N. E., 2011, Handbook of Atomization and Sprays: Theory and Applications. Springer, New York.
[16] Faeth, G. M., 1977, "Current Status of Droplet and Liquid Combustion," Prog. Energy Combust. Sci., **3**(4), pp. 191–224.
[17] Tseng, C. C., and Viskanta, R., 2005, "Effect of Radiation Absorption on Fuel Droplet Evaporation," Combust. Sci. Technol., **177**(8), pp. 1511–1542.
[18] Godsave, G. A. E., 1953, "Burning of Fuel Droplets," Fourth Symposium (International) on Combustion, Vol. 4, Williams and Wilkins, Baltimore, MD, pp. 818–830.
[19] Lefebvre, A. H., and Ballal, D. R., 2010, Gas Turbine Combustion: Alternative Fuels and Emissions, CRC Press, New York.
[20] El-Shanawany, M. S., and Lefebvre, A. H., 1980, "Airblast Atomization: Effect of Linear Scale on Mean Drop Size," J. Energy, **4**(4), pp. 184–189.
[21] Liu, H., 1999, Science and Engineering of Droplets: Fundamentals and Applications. Noyes Publications, Norwich, NY.
[22] Lefebvre, A., 1988, Atomization and Sprays, CRC Press, New York.
[23] Röhl, O., and Peters, N., 2009, "A Reduced Mechanism for Ethanol Oxidation," 4th European Combustion Meeting (ECM 2009), Vienna, Austria, April 14–17, pp. 14–17.
[24] Lefebvre, A. H., 1984, "Flame Radiation in Gas Turbine Combustion Chambers," Int. J. Heat Mass Transfer, **27**(9), pp. 1493–1510.
[25] Lefebvre, A. H., 1980, "Airblast Atomization," Progress Energy Combust. Sci., **6**(3), pp. 233–261.
[26] Gepperth, S., Koch, R., and Bauer, H.-J., 2013, "Analysis and Comparison of Primary Droplet Characteristics in the Near Field of a Prefilming Airblast Atomizer," ASME Turbo Expo, San Antonio, TX, June 3-7, ASME Paper No. GT2013-94033.
[27] Maqua, C., Castanet, G., Grisch, F., Lemoine, F., Kristyadi, T., and Sazhin, S. S., 2008, "Monodisperse Droplet Heating and Evaporation: Experimental Study and Modelling," Int. J. Heat Mass Transfer, **51**(15–16), pp. 3932–3945.
[28] Lavieille, P., Lemoine, F., Lavergne, G., and Lebouche, M., 2001, "Evaporating and Combusting Droplet Temperature Measurements Using Two-Color Laser-Induced Fluorescence," Exp. Fluids, **31**(1), pp. 45–55.
[29] Goldsmith, M., 1955, "The Burning of Single Drops of Fuel in Oxidizing Atmospheres," Ph.D. dissertation, California Institute of Technology, Pasadena, CA.
[30] Wood, B. J., and Wise, H., 1957, "Measurement of the Burning Constant of a Fuel Drop," J. Applied Phys., **28**(9), pp. 1068–1068.